Monthly Notices
of the
ROYAL ASTRONOMICAL SOCIETY

MNRAS **544,** 1–12 (2025)
Advance Access publication 2025 September 23

https://doi.org/10.1093/mnras/staf1597

# The non-uniform expansion of the Crab Nebula

T. Martin ,[1,2]★ D. Milisavljevic,[3,4] T. Temim,[5] S. Mandal,[6,7] P. Duffell,[3] L. Drissen[1] and Z. Ding[3]

[1] *Département de physique, de génie physique et d'optique, Université Laval, 1045 avenue de la médecine, Québec QC G1V 0A6, Canada*
[2] *Cégep Garneau, 1660 Boulevard de l'Entente, Québec QC G1S 4S3, Canada*
[3] *Department of Physics and Astronomy, Purdue University, 525 Northwestern Avenue, West Lafayette, IN 47907, USA*
[4] *Integrative Data Science Initiative, Purdue University, West Lafayette, IN 47907, USA*
[5] *Department of Astrophysical Sciences, Princeton University, 4 Ivy Ln, Princeton, NJ 08544, USA*
[6] *Department of Astronomy, University of Virginia, 530 McCormick Road, Charlottesville, VA 22904, USA*
[7] *Virginia Institute for Theoretical Astronomy, University of Virginia, Charlottesville, VA 22904, USA*

Accepted 2025 September 1. Received 2025 September 1; in original form 2025 February 27

## ABSTRACT

We present extensive proper motion measurements of the Crab Nebula made from Canada–France–Hawaii Telescope MegaPrime/MegaCam images taken in 2007, 2016, and 2019. A total of 19974 proper motion vectors with uncertainty $<10$ mas yr$^{-1}$ located over the majority of the Crab Nebula are used to map the supernova remnant's two-dimensional expansion properties that reflect the dynamics of the original explosion, acceleration of ejecta imparted by spin-down energy from the pulsar, and interaction between the ejecta and surrounding cicumstellar material (CSM). The average convergence date we derive is 1105.5±0.5 CE, which is 15–35 yr earlier compared to most previous estimates. We find that it varies as a function of position angle around the nebula, with the earliest date and smallest proper motions measured along the equator defined by the east and west bays. The lower acceleration of material along the equatorial plane may be indicative of the supernova's interaction with a disc-like CSM geometry. Comparing our measurements to previous analytical solutions of the Crab's expansion and our own numerical simulation using the moving mesh hydrodynamics code SPROUT, we conclude that the ejecta have relaxed closer to homologous expansion than expected for the commonly adopted pulsar spin-down age of $\tau \sim 700$ yr and a pulsar wind nebula (PWN) still evolving inside the flat part of the ejecta density profile. These findings provide further evidence that the PWN has reached the outer steep part of the supernova ejecta density profile and escaped the confines of the ejecta shell in some regions.

**Key words:** methods: data analysis – pulsars: individual: PSR B0531+21 – supernovae: individual: SN 1054 – ISM: supernova remnants.

## 1 INTRODUCTION

The first measurement of the expansion of the Crab Nebula was made by Duncan (1921), following the first detection of changes in the structure of the supernova remnant (SNR) made by Lampland (1921) who used a series of photographs taken with the 40-inch Lowell reflector between 1913 and 1921. The displacement of 12 bright features among the brightest filaments of the nebula were measured on two photographs obtained 11.5 yr apart at the Mount Wilson reflector (the first one by Ritchey in 1909 and the other one by Duncan in 1921). A maximum displacement of 0.17 arcsec yr$^{-1}$ was measured, but the directions of the proper motion vectors appeared scattered, making it impossible to determine a unique centre of expansion (CoE). A second attempt made 18 yr later by Duncan (1939) based on the measurement of the displacement of 20 points between the 1909 photograph and a new photograph obtained in 1939 at the same observatory, clearly showed a general outward expansion and allowed for the first computation of an outburst date of 1172 CE, as well as a first estimate of the distance that yielded 4200 light-years.

Even though the spatial coincidence of the Crab Nebula with a Chinese guest star observed in 1054 CE and reported in the translation of the book 294 of the great Ma-touan-lin collection by Biot (1846) was first suggested by Lundmark (1921) and Hubble (1928), the clear identification of the 1054 CE event with the Crab Nebula and a proof that 'a supernova outburst is accompanied by the throwing off of gaseous shell' came with the articles of Duyvendak & Oort (1940) and Duyvendak (1942) since the time coincidence was supported by the now seminal work of Duncan (1939). Since the book of Stephenson & Green (2002), this explosion date is widely accepted (see e.g. Gaensler & Slane 2006; Hester 2008).

The remarkable work of Trimble (1968) (thereafter T68) is the next major step in the study of the expansion of the Crab Nebula. The use of a filter centred on the H $\alpha$ and [N II] $\lambda\lambda$6548, 6583 lines enhanced the visibility of the filaments, permitting the accurate measurement of the proper motion of 132 features, mostly selected in the outer part of the filamentary shell of the SNR. The proper motion analysis was based on the comparison of two pairs of plates taken 14 yr apart (1939–1953 and 1950–1964). Along with these data, the first 3D velocity data set resulting from the combination of proper motions and radial velocities (measured via spectroscopy) of 127 features was analysed. The distance estimate of around 2 kpc was the best to date,

---

★ E-mail: tmartin@cegepgarneau.ca

and demonstrated that the filamentary complex was not ‘confined to a thin ellipsoid’. Although an outburst date of about 1140 CE could be calculated since the proper motion vectors do converge generally to the same centre of origin, the precision of the measurements also revealed ‘some sort of non-uniformity’ and that ‘it is, therefore, only approximately true that the velocity of each filament is proportional to its distance from the expansion centre’.

Nugent (1998) (thereafter N98) used four scans of high-resolution photographs published between 1939–1992 (three of them found in issues of Sky & Telescope and one provided by the Lick Observatory public information office). The proper motions of 50 features were analysed to find an outburst date of 1130 CE. From a reanalysis of the same data set in a Bayesian framework, Bietenholz & Nugent (2015, thereafter BN15) calculated a value of 1091 CE, somewhat nearer the supernova explosion date of 1054 CE.

Wyckoff & Murray (1977) (thereafter WM77), N98, Kaplan et al. (2008) (thereafter K08) and BN15, all draw similar conclusions, although the location of the explosion centre differs by a few arcseconds (N98, K08). From the analysis made by T68 and N98 (reanalysed later by Bietenholz & Nugent 2015), the homologous expansion of the outburst appears to be well established. However, in all these works, only a few filaments, mostly located on the border of the remnant (where the proper motion is larger), were considered. The one exception is work by Rudie, Fesen & Yamada (2008), who measured proper motions for 35 locations in the northern filamentary jet. In that case, an age of 1055 ± 24 CE was estimated, which they interpret as evidence that the jet experienced less outward acceleration from the central pulsar’s rapidly expanding synchrotron nebula when compared to the main body of the remnant.

In this paper, we conduct our own proper motion measurements of the Crab Nebula. Our original motivation was to investigate in detail the validity of the homologous expansion model (see for example WM77; N98; Bietenholz & Nugent 2015) described below (equation 1) and used by Martin, Milisavljevic & Drissen (2021) to project the ∼400 000 radial velocity points obtained with SITELLE (Drissen et al. 2019) in the Euclidean space. This model is simply based on an unaccelerated motion of the ejected material which means that the velocity of the material, i.e. its proper motion $\mu$ in the celestial plane, is strictly proportional to its distance to the CoE $r$,

$$\mu = \frac{r}{t}\ , \tag{1}$$

where $t$ is a measure of the expansion age (WM77). If the material is truly not accelerated this expansion age should correspond to the time elapsed since 1054 CE. The idea behind Martin et al. (2021) reconstruction is that, from this model, and measuring the mean expansion factor at a certain time, one can infer the velocity in the celestial plane from the distance of the material to the expansion centre. From there, each radial velocity point can be combined to an estimated velocity in the celestial plane to obtain a set of 3D velocity vectors that can then be used to estimate their position in space knowing the outburst date and the distance to the Crab. However, if this expansion is not homologous, i.e. if the material is accelerated in some directions, the overall shape of the SNR computed by Martin et al. (2021) may be substantially different.

Obtaining a precise and complete mapping of the expansion may furthermore offer the possibility to study the acceleration inhomogeneities of the supernova material which may give insights on the dynamics in play since the initial outburst.

## 2 DATA

We have selected three sets of observations taken with Canada–France–Hawaii Telescope (CFHT) MegaPrime/MegaCam instrument through two similar red filters (r and rS) in 2007, 2016, and 2019 (see Fig. 1). Even if multiple exposures were taken we have decided not to combine them so as to avoid additional distortions. In the 2019 data set we have selected the image number 2434 157 because the whole remnant fits in one chip. In the 2007 set, the Crab Nebula is always split between two different chips (see Fig. C1). We therefore selected two different images (906610 and 905816) that show a small overlap. The image quality of the two sets of images is comparable and found to be around 0.8 arcsec (see Table 1).

## 3 ANALYSIS OF THE PROPER MOTION OF THE WHOLE NEBULA

Using the algorithm described in Appendix A, a total of 22 957 proper motion vectors were computed at positions defined from a grid covering the whole remnant with a step size of 7 pixels (1.3 arcsec) from which only positions in the filamentary regions (derived from the H $\alpha$ map obtained with SITELLE and analysed in Martin et al. 2021) and sufficiently far from the stars (*Gaia* DR3 catalogue Gaia Collaboration 2016, 2023) were considered.

We applied two filters to remove vectors associated with weak emission along the outer parts of the remnant and image defects (e.g. hot pixels). The first one is based on the comparison of the proper motion obtained from the 2016–2007 and 2019–2007 sets. The 2359 vectors deviating by more than 5 times the uncertainty calculated in Section A4 were removed. The second filter is based on the hypothesis that the computed vectors should roughly follow a homologous law ($\mu \propto r$). 624 vectors deviating by more than 5 times the standard deviation of the distribution around a fit to this law were also removed. Following this, 19 974 proper motion vectors were retained. The proper motion map obtained is shown in Fig. 2.

### 3.1 Centre of expansion and expansion age

Two methods have been used by different authors to calculate the expansion age of the SNR and the position of its CoE. Both methods are based on a constant velocity uniform expansion model (see equation 1), which has been largely proven to be inappropriate since the resulting outburst date is always calculated to be later than the canonical 1054 CE by a hundred years (see Duncan 1921; Bietenholz & Nugent 2015 and the more recent calculated outburst dates reported in Table 2).

The first method, used by T68 consists in computing the time of closest approach in the least-square sense. Given the position and proper motion of some vectors, one can calculate backward their position and find the moment where they cover the smallest region in the sky. The mean position of the vectors at this time gives the position of the expansion centre. We have written this algorithm and compared its results to the results obtained on the same data by T68 to verify that our implementation was correct.

The second method, used by WM77 and N98, relies on the least-square fit of an unaccelerated expansion model (see equation 1) relating the proper motion ($\mu_\alpha$, $\mu_\delta$) to the right ascension and declination coordinates with respect to the Duncan reference star ($\Delta\alpha$, $\Delta\delta$)

$$\mu_\alpha = t^{-1}\Delta\alpha\ , \tag{2}$$

$$\mu_\delta = t^{-1}\Delta\delta\ . \tag{3}$$

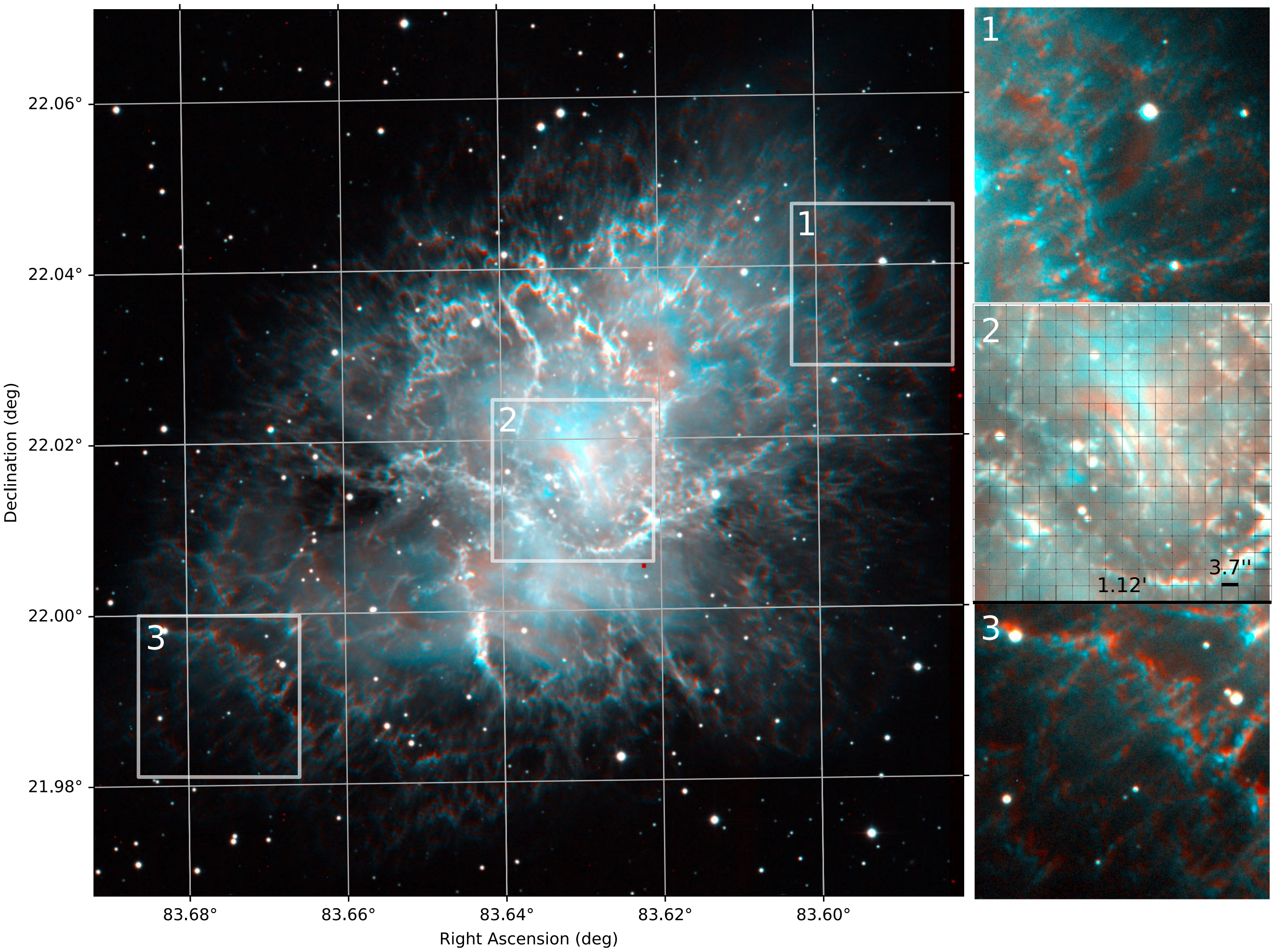

**Figure 1.** Combination of the images taken in 2007 (red) and 2016 (blue) with three zoomed-in regions on the right. The expansion of the SNR is conspicuous. We added a grid on region 2 to show the size of the tiles compared to compute the proper motion (see Section A).

**Table 1.** Images compared to compute the proper motion. They were all obtained with MegaPrime/MegaCam at the CFHT.

| Image number | Chip | Exposure date | Filter | FWHM (') |
|---|---|---|---|---|
| 2434157 | 22 | 2019 July 9 | r | 0.7 |
| 1892362 | 22 | 2016 Feb 7 | r | 1.0 |
| 906610 | 20 | 2007 Apr 13 | rS | 0.9 |
| 905816 | 21 | 2007 Apr 13 | rS | 0.7 |

*Notes.* Plate scale: 0.1869 arcsec pixel$^{-1}$.
Time span of the 2016–2007 set: 8.83 yr (3224 jd).
Time span of the 2019–2007 set: 12.24 yr (4472 jd).

The resulting fit on our data is shown on Fig. 3.

The results obtained with both methods are presented in Table 2 and Fig. 4. The uncertainties on these values were computed with a bootstrap method in which the parameters are recomputed a thousand times with the data points each time shifted by a random value sampled from a Normal distribution reflecting the systematics and random uncertainties quoted in Table A2.

We found nearly the same positions of the CoE with both methods (see Table 2), but our calculated outburst date is very different from the date obtained with the other method. Note that the same discrepancy was already observed by WM77 when they applied the second method to the data obtained by T68. We favour the results obtained with the fit method since it is much easier to implement and seems, in this way, more statistically robust. As an example, with the closest approach method, the region occupied at the closest approach time is, in fact, very large (the 1$\sigma$ diameter of this region is around 20 arcsec) because the proper motion uncertainty projected a thousand years back is large. This added step of backward projection may influence the statistics of the computed expansion date in some ways that are more difficult to control. Given the fact that, in principle, both methods should give the same results, we favour the simplest of both.

We have also estimated the position of the CoE and the expansion age considering only the 20 per cent brightest regions. We used the map of the filaments obtained with SITELLE (see Martin et al. 2021) to consider only the filamentary regions containing the smallest portion of continuum flux. In this case, the outburst date (1121.4 ± 1.5 CE) is found between our results considering the whole nebula and the results from the previous studies. Because the brightest regions are more generally found in the west part of the nebula, the CoE is slightly displaced to the west.

Although our estimation of the CoE is based on much more data than the previous works, our quoted uncertainties are not appreciably better. The main reason comes from the systematics discussed in Section A3. If the systematic uncertainties are set to

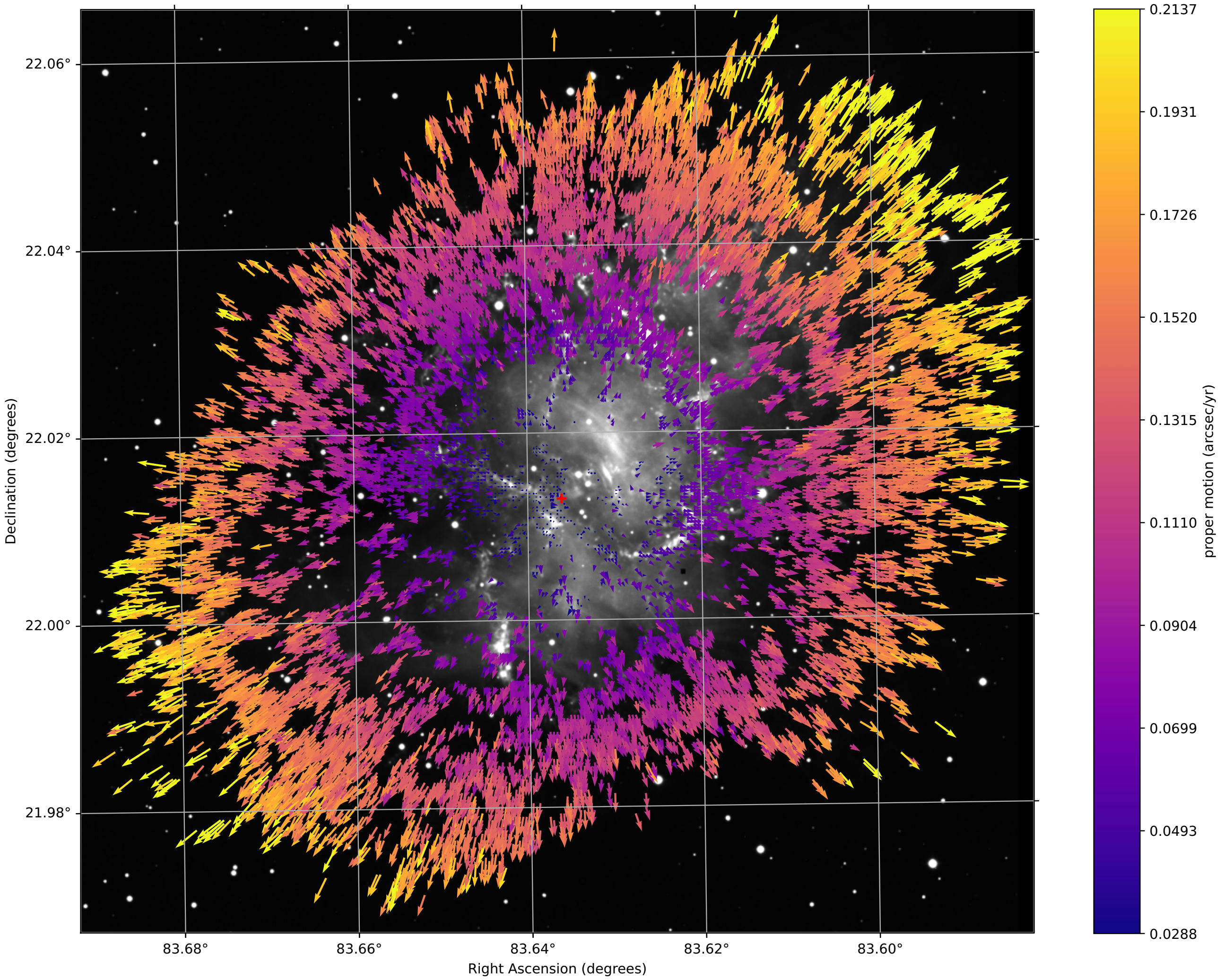

**Figure 2.** Proper motion vectors measured on the filamentary regions of the Crab Nebula from our Megacam images. For a more readable representation, only half of all 19 974 vectors are shown. The background image is the 2019 observation. The arrows point to the position the material will occupy in 50 yr from now. The central cross (in red) is our derived CoE.

zero the estimated uncertainties on the position of the CoE fall down to 0.05 arcsec.

### 3.2 2D expansion properties

The quality of our measurements allowed us to go beyond a straightforward average of the proper motions of all data and investigate how expansion properties of the Crab may change as a function of position angle from the CoE. We divided the remnant into 20 angular wedges originating from the CoE, then re-ran the same procedure outlined in Section 3 using the data from these wedges. The results are shown in Fig. 5. There is considerable difference in the inferred outburst date among the radial segments. The youngest ages are found in the north and south, whereas the oldest ages consistent with the least amount of acceleration are found in the east and west. The maximum age of 1115 C.E. is in the north-west region where ‘breakout’ of the radio synchrotron nebula is observed (Sankrit & Hester 1997). Clearly, this morphology was imprinted on the nebula’s kinematics by the strong relativistic wind along the pulsar’s rotation axis.

The smallest proper motions are measured along the equator defined by the east and west bays (around position angles 90 and 270 degrees). These small proper motions are consistent with radial velocity measurements from published optical spectra showing conspicuously reduced ejecta velocities ‘pinched’ in these regions (Lawrence et al. 1995; Fesen, Shull & Hurford 1997). This arrested expansion, along with enhanced helium abundances in filaments in these regions (MacAlpine et al. 1989; Fesen et al. 1997; Satterfield et al. 2012), may be indicative of interaction with a concentration of circumstellar material (CSM) that impeded the expansion (Fesen, Martin & Shull 1992; Smith 2013).

The presence of a pre-SN CSM that the blast wave and ejecta ran into and interacted with shortly after core collapse has been proposed to help explain the unusually high luminosity of the original supernova (−18 mag; Stephenson & Green 2002) that produced the Crab Nebula reported in historical records, which stands in contradiction with the surprisingly low kinetic energy ($\approx 7 \times 10^{49}$ erg) inferred from the total ejecta observed now (see e.g. Chugai & Utrobin 2000). None the less, other interpretations for the high luminosity exist (see e.g. Tominaga, Blinnikov & Nomoto 2013; Omand, Sarin & Temim 2024), as well as an interpretation that the east-west filaments appear particularly prominent due to projection effects (Hester et al. 1995).

**Table 2.** Expansion centres computed by different authors (and compiled by N98 and K08) including the positions computed in this work with (1) a fit on the proper motion versus position graph (chosen as a reference in this article) and (2) the closest approach method. The positions are calculated with respect to the Duncan (1921) reference star. See Fig. 4 for a map of these positions. The resulting outburst date considering an unaccelerated expansion is also reported.

| Reference method | $\Delta\alpha$ ($''$) | $\Delta\delta$ ($''$) | Date |
|---|---|---|---|
| **This work**[a] | **6.9(0.8)** | **−9.3(0.9)** | **1105.5(0.5)** |
| This work[b] | 6.7(0.8) | −8.8(0.9) | 1140.5(1.4) |
| This work (brightest)[a] | 5.9(0.8) | −9.0(0.8) | 1121.4(1.5) |
| T68[b] | 7.6(1.3) | −8.5(1.1) | 1140(15) |
| WM77[a] (T68 data) | 6.9(0.9) | −7.4(0.9) | 1120(7) |
| N98[a] | 9.4(1.7) | −8.0(1.3) | 1130(16) |
| BN15[a] (N98 data) | 15.3 | −9.2 | 1091(34) |
| BN15 (synchrotron) | – | – | 1255(27) |
| K08[c] | 7.9(0.4) | −8.1(0.4) | |
| *Gaia* DR3[c] | 7.8(0.1) | −6.02(0.06) | |

*Notes.* [a]Fit on a proper motion versus position graph (retained as a reference).
[b]Closest approach method.
[c]Computed position of the pulsar in 1054 CE based on its measured proper motion.

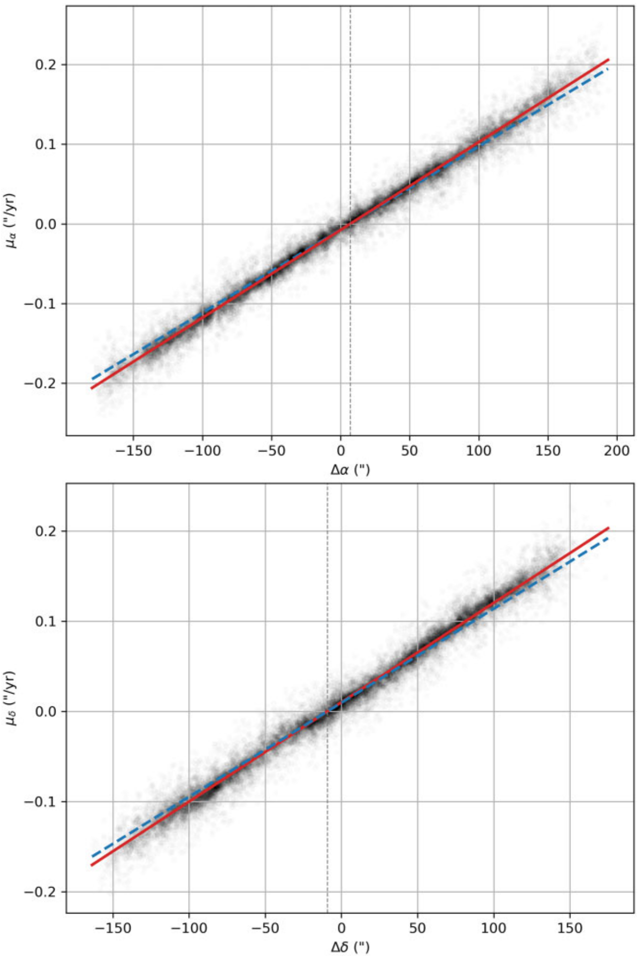

**Figure 3.** Proper motion versus position with respect to the Duncan (1921) reference star along right ascension (top) and declination (bottom). The solid line (in red) shows the result of a least square fit using the unaccelerated model of equations (2) and (3). The dashed line (in blue) illustrates the result of an unaccelerated expansion since 1054 CE.

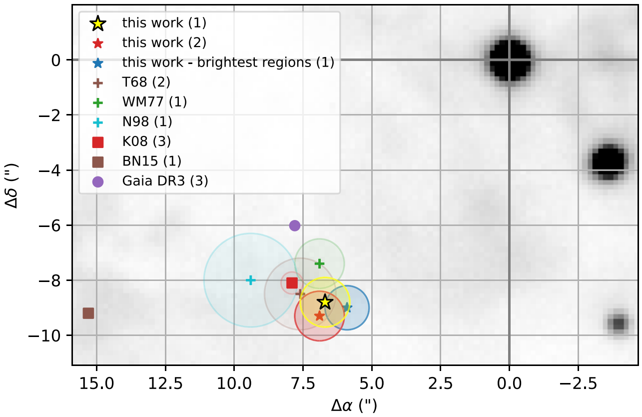

**Figure 4.** Map of the expansion centres computed by different authors and reported in Table 2 including the position computed in this work with (1) a fit on a proper motion versus position graph (chosen as a reference in this article) and (2) the closest approach method. $1\sigma$ uncertainties are shown as circles. The arrow and the dashed grey line indicate the direction of the proper motion of the Crab pulsar computed by K08. The positions are shown with respect to the Duncan (1921) reference star located at (0,0).

Some 3D magnetohydrodynamic models predict an elongation of the pulsar wind nebula (PWN) along the pulsar's rotation axis (Olmi et al. 2016), that may result in anisotropic acceleration of the ejecta filaments. However, we measure least accelerated material along the east–west direction and not along the torus axis, as would be expected in that scenario. Temim et al. (2024) highlight numerous indentations along the perimeter of the synchrotron nebula, including the most prominent east and west bays, and suggest that all may be due to confinement of the PWN by prominent ejecta filaments. As seen in Fig. 5, we find that expansion tends to be less accelerated in the directions of the indentations noted by Temim et al. (2024), particularly along the east and west bays, but exceptions are seen (e.g. a south-west indentation coincides along a direction where the estimated outburst date is among the youngest measured). A definitive proof for significant CSM material is still lacking, but future analysis of the kinematic and chemical properties of the Crab Nebula in 3D enabled by multiple epochs of SITELLE observations could provide the necessary confirmation. Indeed, it may be that the inhomogeneous acceleration of material is due to a combination of confinement by both ejecta filaments and CSM.

## 4 NUMERICAL MODELLING

From the assumption that the supernova outburst took place in 1054 C.E., the actual proper motion is too fast to be explained with a ballistic, homologous expansion ($v = r/t$, see Fig. 6). Instead, the younger inferred explosion date may be explained by taking into account the wind driven by the central pulsar, which accelerates the ejecta. Let us consider a spherically symmetric pulsar wind expanding into the ejecta, which has uniform density in the interior. In this case, the wind-accelerated ejecta can be shown analytically to evolve in size as $r \propto t^{6/5}$ (using dimensional analysis; also see Chevalier 1977) instead of $r \propto t$ (as for free expansion).

This will lead to an expansion velocity $v$ greater than $r/t$:

$$v = \dot{r} \propto \frac{\mathrm{d}(t^{6/5})}{\mathrm{d}t} = \frac{6}{5} t^{1/5} . \qquad (4)$$

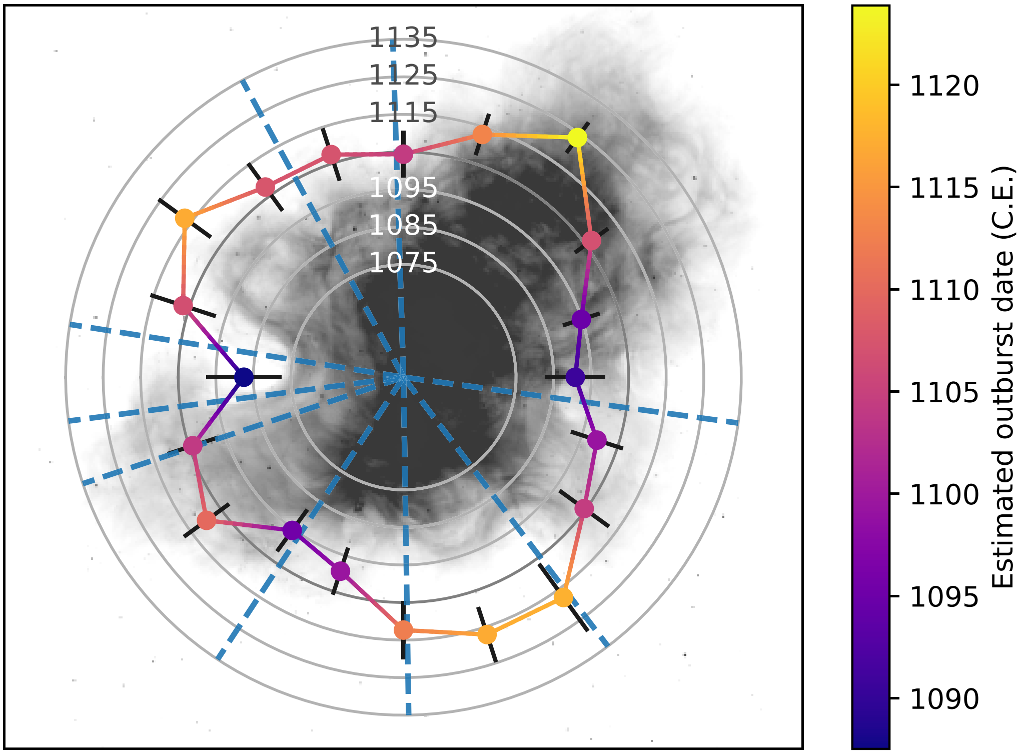

**Figure 5.** Inferred outburst date as a function of position angle. Each point is the outburst date computed by taking the points contained in small angular wedges around the nebula. The uncertainty is indicated by black error bars. The darker grey line demarcates the radial distance corresponding to our inferred outburst date using all data. The dashed lines indicate the directions of the bays found by Temim et al. (2024). The background image is a *James Webb Space Telescope* continuum map published in Temim et al. (2024).

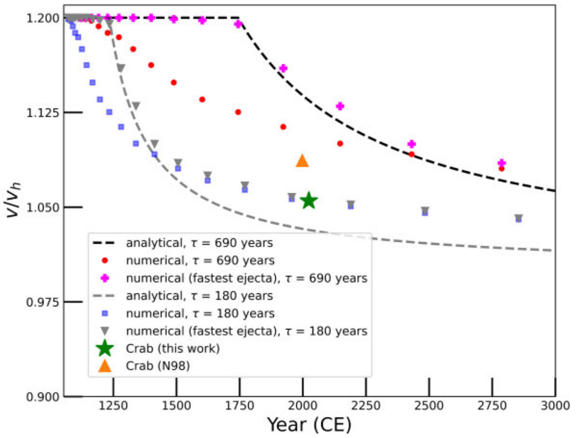

**Figure 6.** The ratio of the observed velocity $v$ and ballistic homologous expansion velocity $v_{\rm h} = r/t$ (also the ratio of the real age to the inferred age of the PWN) as a function of time. The star (in green) shows the mass-unweighted average measured in this paper.

We can derive how much faster this is with respect to $v_{\rm h}$, the velocity corresponding to ballistic, homologous expansion:

$$v_{\rm h} = \frac{r}{t} \propto \frac{t^{6/5}}{t} = t^{1/5} \tag{5}$$

which leads to

$$v = \frac{6}{5} v_{\rm h}. \tag{6}$$

This equation assumes the power supplied by the wind to be constant. However, owing to spin-down of the pulsar, the wind loses power. A significant fraction of the wind power is lost by the spin-down age ($\tau$) of the pulsar (see equation 3 of Yang & Chevalier 2015 for the exact definition). This implies that the ejecta in the PWN should relax to homologous expansion after this time-scale. Using equation (6), the velocity at $t = \tau$ is

$$v = \frac{6}{5} \frac{r_0}{\tau}, \tag{7}$$

assuming the size of the PWN to be equal to $r_0$ at $t = \tau$. When the age of the PWN becomes greater than the spin-down age, the PWN can no longer be accelerated by the pulsar wind and expands ballistically. In other words, $r(t > \tau) = r_0 + v(t - \tau)$. Eliminating $r_0$ using equation (7), this can be written as an expression for the velocity of the ejecta after the pulsar has started spinning down:

$$v = \left(1 - \frac{\tau}{6t}\right)^{-1} \frac{r}{t} = \left(1 - \frac{\tau}{6t}\right)^{-1} v_{\rm h}. \tag{8}$$

Equations (6) and (8) give us an analytical prediction of the ratio between the observed velocity $v$ and homologous expansion velocity $v_{\rm h}$ in a PWN, given the spin-down age $\tau$ is known. The ratio $v/v_{\rm h}$ is also the ratio of the real age to the inferred age of the PWN ($v = r/t' = (t/t')(r/t) = (t/t')v_{\rm h}$, where $t'$ is the inferred age assuming unaccelerated expansion). It can be seen from equation (8) that $v/v_{\rm h}$ approaches unity as the age of the pulsar increases ($\tau \ll t$), or the ejecta assumes homologous expansion after the pulsar has had sufficient time to spin-down.

We can also calculate $v/v_{\rm h}$ using a 3D numerical PWN model. This model was developed using SPROUT (Mandal & Duffell 2023), a finite volume moving mesh hydrodynamics code with second order accuracy. SPROUT solves the equations of ideal, non-relativistic hydrodynamics on a Cartesian mesh that can expand self-similarly with time. The model is designed to test the idea that the Crab resulted from a SN with atypically low energy (Yang & Chevalier 2015), and that the pulsar wind is still inside the dense, inner part of the stellar ejecta (Hester 2008). This would require freely expanding ejecta beyond the visible Crab, which is considered unlikely (Frail et al. 1995; Fesen et al. 1997; Seward, Tucker & Fesen 2006), but cannot be ruled out firmly due to blueshifted UV absorption lines seen around the Crab, albeit accounting for only 0.3 $\mathrm{M}_\odot$ of material (Sollerman et al. 2000; but see also Lundqvist & Tziamtzis 2012). We start from a homologously expanding ejecta, with a mass of $5\mathrm{M}_\odot$, and an ejecta energy of $10^{50}$ ergs. The ejecta density profile is chosen to be a double power law, with a constant density inner ejecta and steeply declining density ($\rho \propto r^{-9}$) in the outer ejecta. Calculations start at 1 month, and continue up to the present age of the Crab. The wind from the central pulsar is taken to be spherically symmetric, with the luminosity given by:

$$L(t) = L_0 \left(1 + \frac{t}{\tau}\right)^{-\frac{n+1}{n-1}}, \qquad (9)$$

where $L_0 = 10^{39}$ ergs/s, the pulsar braking index $n = 2.51$ (Lyne et al. 2015) and $\tau = 690$ yrs (using equation 3 of Yang & Chevalier 2015 and parameters of the Crab pulsar from Lyne et al. 2015). These parameters ensure that the pulsar has spun down significantly at the present age of the model, and that the wind still remains confined by the constant density inner ejecta. We obtain proper motion of the shocked plasma in the model in the plane of the sky as a function of the radial coordinate in the sky (similar to Fig. 6). This data provides $v/v_\mathrm{h}$ as a function of the pulsar age $t$.

The analytical and numerical values of $v/v_\mathrm{h}$ are shown in Fig. 6, along with the average value of $v/v_\mathrm{h} = 1.06$ we derive for the Crab from our proper motion measurements. Note that we don't attempt to measure $v/v_\mathrm{h}$ using the closest approach method because the position of the proper motion vectors cannot be traced back to the same origin and therefore equations (6) or (8) do not remain valid.

Fig. 6 indicates the Crab nebula has relaxed closer to homologous expansion than indicated by the analytical or numerical models. Thus, the inner ejecta confined pulsar wind model of Yang & Chevalier (2015), with a spin-down age of 690 years, fails to explain the observed proper motion in the Crab.

One way to interpret this discrepancy is that the wind has already blown through the inner ejecta and has made its way to the steeply dropping outer ejecta, as suggested by Blondin & Chevalier (2017). In this phase, the PWN no longer remains self-similar, since hydrodynamic instabilities produce cracks or channels in the shocked shell, and the pulsar wind escapes through these channels. This could slow down the filaments more than in the self-similar case, since the wind blows through the shocked shell and cannot accelerate it as effectively as before.

In such a case, one would expect the wind (emitting synchrotron radiation at radio wavelengths) to have a considerably larger $v/v_\mathrm{h}$ ratio than the dense filaments seen in the optical. In fact, Bietenholz & Nugent (2015) measured multiple epochs of VLA 5 GHz radio images of the Crab and calculated $v/v_\mathrm{h} = 1.26$ for the Crab synchrotron nebula (see Table 2). If we consider the fast moving shocked plasma closest to the forward shock in our numerical model to be representative of the shocked wind and calculate $v/v_\mathrm{h}$ only for this plasma, we obtain a curve that almost exactly matches the analytical prediction (equations (6) and 8) in Fig. 6. Thus, at Crab's present age, we should expect a $v/v_\mathrm{h}$ close to 1.15. The fact that it is greater than 1.2 is suggestive of a blowout, or perhaps a shallow density profile of the inner ejecta (say $\rho \propto r^{-1}$) instead of constant density.

We also explored an alternative model, where the spin-down age is assumed to 180 yr (blue squares in Fig. 6), which is much less than the typically adopted age of 690 yr, and higher initial luminosity. This is motivated in part by recent modelling of historical and contemporary light curves of the Crab that consider a significantly smaller spin-down age of the pulsar (Omand et al. 2024). Although typical estimates of the spin-down age are based on the assumption that the spin period of a pulsar evolves as a power-law (with a constant index) after it starts spinning down (see Yang & Chevalier 2015), and this power-law index has been observed to be fairly constant ($\sim 2.51$) for the past 50 yr (Lyne & Graham-Smith 1998; Lyne et al. 2015), Lyne et al. (2015) show that the Crab exhibits 'glitches' which are essentially large but short-duration deviations from a simple power law evolution.

We find close overlap between the $v/v_\mathrm{h}$ of our 180 yr model and the proper motion-derived estimate reported in this paper. None the less, many caveats are noted for this interpretation. First, the proper motion measurements from our numerical model take into account all of the shocked plasma, yet it is unclear if all the shocked plasma in the Crab is bright enough to be included in the presented optical proper motion measurements. This is a factor that could influence the curve for the numerical model. Secondly, the wind from the Crab pulsar is not symmetric but equatorial and also includes a bipolar jet (see for example X-ray images of the Crab; Weisskopf et al. 2000 and Mizuno et al. 2023). Likewise, the environment into which the supernova expanded into may have included a circumstellar disc (Fesen et al. 1992; Smith 2013). It is possible that the ratio $v/v_\mathrm{h}$ will evolve somewhat differently for such a system. Furthermore, reproducing the radio convergence date reported in Bietenholz & Nugent (2015) would require adoption of a different ejecta profile (e.g. $\rho \propto r^{-1}$). Finally, the model assumes that the PWN is still expanding into the flatter part of the ejecta density profile, while the observed filament distribution is more consistent with the 'blowout' scenario in which the PWN has reached the steep part of the ejecta profile (e.g. Temim et al. 2024). This investigation is being pursued and will be published in a future study (Mandal et al., in preparation).

## 5 CONCLUSIONS

We have presented proper motion measurements of the Crab Nebula made from three epochs of CFHT images spanning twelve years. Our data set of 19 974 proper motion vectors with uncertainty $<10\,\mathrm{mas\,yr^{-1}}$ spanning the majority of the Crab Nebula is the most extensive and detailed mapping of the Crab's two-dimensional expansion properties to date. The major findings of our analysis are as follows:

(i) We estimate the CoE of the Crab Nebula to be located at $5^\mathrm{h}34^\mathrm{m}32.67^\mathrm{s} + 22^\circ00'46.7''$ (J2000), with $1\sigma$ uncertainty of 1.2 arcsec. This origin is broadly consistent with previous estimates (e.g. T68).

(ii) We calculate the average date of convergence of the ejecta to be 1105.5 CE ± 0.5. Our date is 15–35 yr earlier than most previous estimates, but still consistent with pulsar wind-driven acceleration of ejecta from a historically-recorded supernova explosion date of 1054. Our convergence date is consistent with the optical convergence date reported in Bietenholz & Nugent (2015), but our estimate more faithfully traces the entire remnant using a uniform data set and suffers from less uncertainty.

(iii) We show that the convergence date varies with position angle around the Crab Nebula, and that the greatest age associated with lowest acceleration is measured in the equatorial region aligned with the east–west synchrotron bays. This finding is consistent with an SN ejecta and PWN expansion into a disc-like CSM geometry.

(iv) Comparing our results to previous analytical predictions of the expansion of the Crab Nebula suggests that the ejecta are closer to homologous expansion now than previously thought. We conducted a 3D numerical simulation of this expansion assuming a typically-adopted spin-down age of 690 yr, and verified that the expected $v/v_\mathrm{h}$ is higher than our observed value. Multiple lines of evidence, including the difference in convergence dates for the optical versus radio-emitting components of the Crab (Bietenholz & Nugent 2015), favour that the discrepancy is a consequence of the pulsar wind having already blown through the inner flat part of the ejecta density profile (Blondin & Chevalier 2017). We also explore an alternative possibility that a more rapid spin-down age of 180 yr may be more appropriate for the Crab pulsar, but note many caveats to this interpretation.

Accurate interpretation of the optical convergence date we estimate depends critically on the convergence date estimated from the radio-emitting pulsar wind radiation (Bietenholz & Nugent 2015). An independent measurement of the synchrotron nebula's proper motion and associated convergence date, made via optical or infrared imaging and closely following the asymmetry of the wind, would provide additional valuable information about the origin of the Crab Nebula's expansion dynamics. Also desirable are multiple epochs of SITELLE observations, which would permit proper motion investigations that can mitigate the confusion of multiple velocity components along the line of sight. Such a 3D expansion mapping would enable a more precise 3D rendering of the Crab Nebula than Martin et al. (2021), and have the potential to robustly characterize the surrounding CSM geometry.

## ACKNOWLEDGEMENTS

We are thankful to Marianne Ruest which pointed out the existence of PIV algorithms, and to William Blair who read an earlier draft of the manuscript and provided helpful comments.

We are also thankful to the PYTHON (Van Rossum & Drake 2009) community and the free softwares that made the analysis of this data possible: NUMPY (Oliphant 2006), SCIPY (Virtanen et al. 2020), PANDAS (McKinney et al. 2010), PANDA3D (Goslin & Mine 2004), PYVISTA (Sullivan & Kaszynski 2019), MATPLOTLIB (Hunter 2007), and ASTROPY (Price-Whelan et al. 2018).

Based on observations obtained with MegaPrime/MegaCam, a joint project of CFHT and CEA/DAPNIA, at the CFHT which is operated by the National Research Council (NRC) of Canada, the Institut National des Science de l'Univers of the Centre National de la Recherche Scientifique (CNRS) of France, and the University of Hawaii. The observations at the CFHT were performed with care and respect from the summit of Maunakea which is a significant cultural and historic site. This paper is also based on observations obtained with SITELLE, a joint project of Université Laval, ABB, Université de Montréal and the CFHT, the Institut National des Science de l'Univers of the Centre National de la Recherche Scientifique (CNRS) of France, and the University of Hawaii.

DM acknowledges NSF support from grants PHY-2209451 and AST-2206532. LD is grateful to the Natural Sciences and Engineering Research Council of Canada and the Fonds de Recherche du Québec for funding. TT acknowledges support from the NSF grant AST-2205314 and the NASA ADAP award 80NSSC23K1130.

This work has made use of data from the European Space Agency (ESA) mission *Gaia* (https://www.cosmos.esa.int/gaia), processed by the *Gaia* Data Processing and Analysis Consortium (DPAC, https://www.cosmos.esa.int/web/gaia/dpac/consortium). Funding for the DPAC has been provided by national institutions, in particular the institutions participating in the *Gaia* Multilateral Agreement.

## DATA AVAILABILITY

The data underlying this article will be shared on reasonable request to the corresponding author.

## REFERENCES

Adrian R. J., 1991, Ann. Rev. Fluid Mech., 23, 261
Bietenholz M. F., Nugent R. L., 2015, MNRAS, 454, 2416 BN15
Biot M. É., 1846, Connaissance des temps ou des mouvements célestes à l'usage des astronomes et des navigateurs, Bureau des longitudes. Imprimerie de la République, Paris, France, p. 60
Blondin J. M., Chevalier R. A., 2017, ApJ, 845, 139
Chevalier R. A., 1977, in Schramm D. N., ed., Astrophysics and Space Science Library, Vol. 66, Supernovae, Was SN 1054 A Type II Supernova? Springer, Dordrecht, p. 53
Chugai N. N., Utrobin V. P., 2000, A&A, 354, 557
Drissen L. et al., 2019, MNRAS, 485, 3930
Duncan J. C., 1921, Proc. Natl. Acad. Sci. USA, 7, 179
Duncan J. C., 1939, ApJ, 89, 482
Duyvendak J. J. L., 1942, PASP, 54, 91
Duyvendak J. J. L., Oort J. H., 1940, T'oung Pao, 36, 174
Fesen R. A., Martin C. L., Shull J. M., 1992, ApJ, 399, 599
Fesen R. A., Shull J. M., Hurford A. P., 1997, AJ, 113, 354
Frail D. A., Kassim N. E., Cornwell T. J., Goss W. M., 1995, ApJ, 454, L129
Gaensler B. M., Slane P. O., 2006, ARA&A, 44, 17
Gaia Collaboration, 2016, A&A, 595, A1
Gaia Collaboration, 2023, A&A, 674, A1
Goslin M., Mine M. R., 2004, Computer, 37, 112
Greisen E. W., Calabretta M. R., 2002, A&A, 395, 1061
Hester J. J., 2008, ARA&A, 46, 127
Hester J. J. et al., 1995, ApJ, 448, 240
Hubble E. P., 1928, Leaflet Astron. Soc. Pac., 1, 55
Hunter J. D., 2007, Comput. Sci. Eng., 9, 90
Kaplan D. L., Chatterjee S., Gaensler B. M., Anderson J., 2008, ApJ, 677, 1201 (K08)
Keane R. D., Adrian R. J., 1990, Meas. Sci. Tech., 1, 1202
Lampland C. O., 1921, PASP, 33, 79
Lawrence S. S. et al., 1995, AJ, 109, 2635
Lundmark K., 1921, PASP, 33, 225
Lundqvist P., Tziamtzis A., 2012, MNRAS, 423, 1571
Lyne A. G., Graham-Smith F., 1998, Pulsar Astronomy. Cambridge Univ. Press, Cambridge
Lyne A. G., Jordan C. A., Graham-Smith F., Espinoza C. M., Stappers B. W., Weltevrede P., 2015, MNRAS, 446, 857
MacAlpine G. M., McGaugh S. S., Mazzarella J. M., Uomoto A., 1989, ApJ, 342, 364
Mandal S., Duffell P. C., 2023, ApJS, 269, 30
Martin T., Milisavljevic D., Drissen L., 2021, MNRAS, 502, 1864
McKinney W., et al., 2010, Proceedings of the 9th Python in Science Conference, Data Structures for Statistical Computing in Python. Austin, p. 51
Mizuno T., Ohno H., Watanabe E., Bucciantini N., Gunji S., Shibata S., Slane P., Weisskopf M. C., 2023, PASJ, 75, 1298
Nugent R. L., 1998, PASP, 110, 831 (N98)
Oliphant T. E., 2006, A Guide to NumPy, Vol. 1. Trelgol Publishing, USA

Olmi B., Del Zanna L., Amato E., Bucciantini N., Mignone A., 2016, J. Plasma Phys., 82, 635820601
Omand C. M. B., Sarin N., Temim T., 2024, preprint (arXiv:2404.19017)
Price-Whelan A. M. et al., 2018, AJ, 156, 123
Robitaille T., Deil C., Ginsburg A., 2020, Astrophysics Source Code Library, record ascl:2011.023
Rudie G. C., Fesen R. A., Yamada T., 2008, MNRAS, 384, 1200
Sankrit R., Hester J. J., 1997, ApJ, 491, 796
Satterfield T. J., Katz A. M., Sibley A. R., MacAlpine G. M., Uomoto A., 2012, AJ, 144, 27
Seward F. D., Tucker W. H., Fesen R. A., 2006, ApJ, 652, 1277
Shupe D. L., Moshir M., Li J., Makovoz D., Narron R., Hook R. N., 2005, ASP Conf. Ser. Vol. 347, Astronomical Data Analysis Software and Systems XIV. Astron. Soc. Pac., San Francisco, p. 491
Smith N., 2013, MNRAS, 434, 102
Sollerman J., Lundqvist P., Lindler D., Chevalier R. A., Fransson C., Gull T. R., Pun C. S. J., Sonneborn G., 2000, ApJ, 537, 861
Stephenson F. R., Green D. A., 2002, Historical Supernovae and their Remnants. Clarendon Press, Oxford
Sullivan C. B., Kaszynski A., 2019, J. Open Source Softw., 4, 1450
Temim T. et al., 2024, ApJ, 968, L18
Thielicke W., Stamhuis E. J., 2014, Journal of open research software, 2, e30
Tominaga N., Blinnikov S. I., Nomoto K., 2013, ApJ, 771, L12
Trimble V., 1968, AJ, 73, 535 (T68)
Van Rossum G., Drake F. L., 2009, Python 3 Reference Manual. CreateSpace, Scotts Valley, CA
Virtanen P. et al., 2020, Nat. Methods, 17, 261
Weisskopf M. C. et al., 2000, ApJ, 536, L81
Wyckoff S., Murray C. A., 1977, MNRAS, 180, 717 (WM77)
Yang H., Chevalier R. A., 2015, ApJ, 806, 153

## APPENDIX A: PROPER MOTION COMPUTATION METHOD

The general idea is to estimate the displacement (in pixels) of the features between 2007 and 2016 or 2019 in small 20 pixel-wide boxes (3.7 arcsec × 3.7 arcsec) which can then be translated to a proper motion. Therefore, the compared region must be perfectly aligned and, if possible, free of any significant distortion. The images are thus first registered and aligned (see Section A1). The displacement vectors are computed at different positions on the Crab Nebula (see Section A2) and corrected for the point spread function (PSF) asymmetry and the mean proper motion in this field (see Section A3). Finally the proper motion in celestial coordinates can be calculated (see Section A4).

### A1 Step 1: registration and alignment of the images

Each image was first registered independently using the *Gaia* DR3 (Gaia Collaboration 2016, 2023) catalogue (see Fig. C1). 264 stars were selected in the vicinity of the Crab Nebula. Stars with a large proper motion were removed from the list of stars used. In order to mitigate the effects of large scale distortion the registration was made with a Simple Imaging Polynomial (Shupe et al. 2005) of degree 3 for the images taken in 2007 and of degree 2 for the images taken in 2016 and 2019 which tends to display better optical properties. This degree was found to be the largest needed for an adequate Gaussian distribution of the residuals and small enough to avoid overfitting.

Registration errors are generally below 0.1arcsec (≈0.5 pixel, see Fig. C1), which translate to an uncertainty of 8.17 to 11.3 mas yr$^{-1}$ when comparing images separated by 8.83 and 12.24 yr (see Table 1).

Then the two 2007 fields are projected on the 2019 field (which is used as the reference field in the whole analysis since it is the only

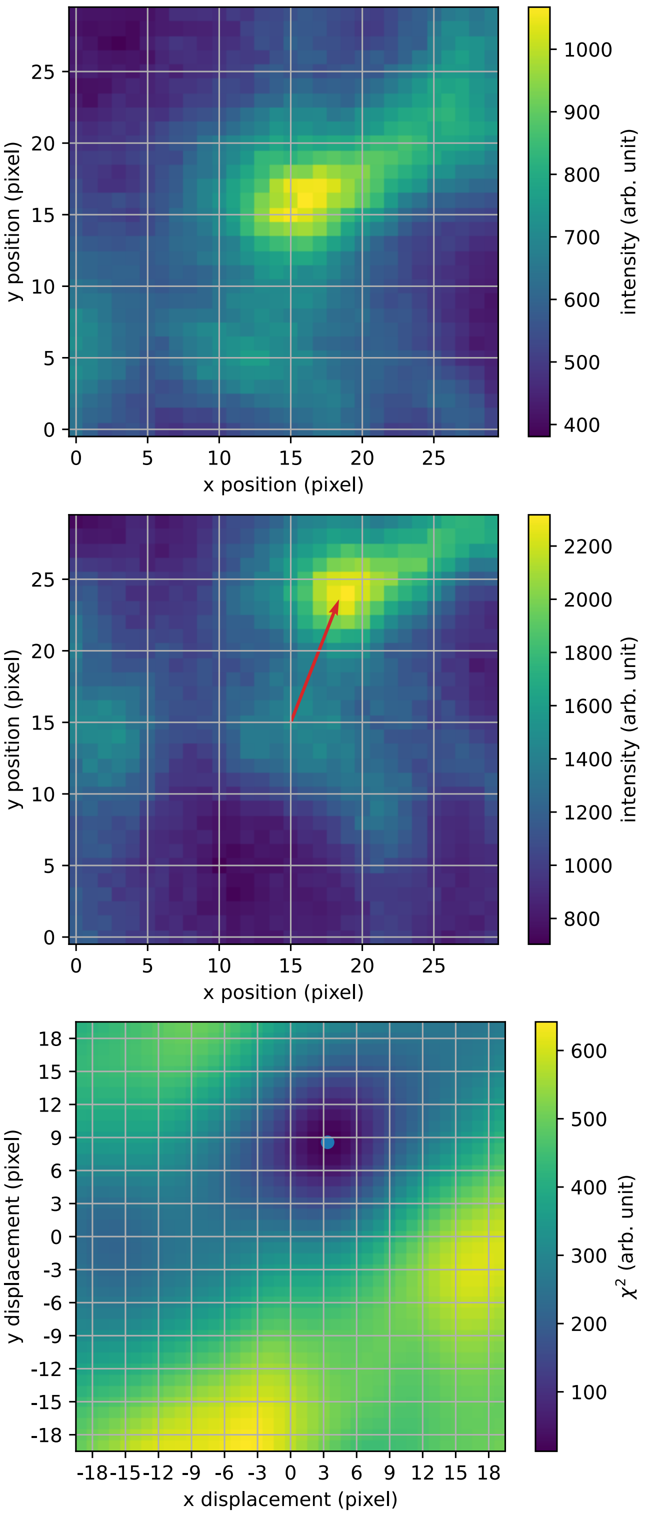

**Figure A1.** (*Top and centre panels*) Example of two compared tiles taken at the same celestial coordinates on the 2007 and 2016 images. The arrow (in red) indicates the estimated displacement vector. *(Bottom panel)* Calculated $\chi^2$ matrix of all the possible shifts tried along the $x$ and $y$ axes. The position of the estimated best shift is located with a dot (in blue).

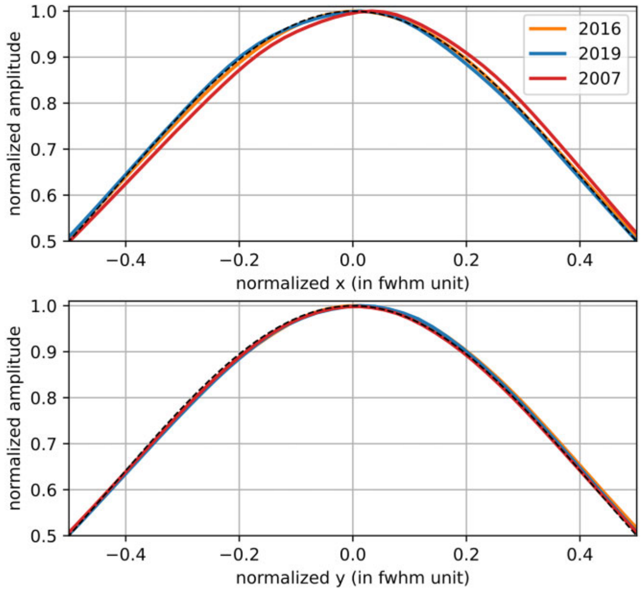

**Figure A2.** Normalized computed PSF of the stars in the compared images. Only the superior part is drawn to better show the asymmetry of the 2007 PSF along the $x$ axis which leads to a non-negligible systematic on the computed proper motion along the RA axis.

**Table A1.** Systematics estimated (and corrected) caused by the mean proper motion of the reference stars and the PSF asymmetries.

| Sets | Mean proper motion | | PSF asymmetry | |
|---|---|---|---|---|
| | $\Delta\alpha$ mas | $\Delta\delta$ mas | $\Delta\alpha$ mas | $\Delta\delta$ mas |
| 2007–2016 | 5.15(16) | 9.88(10) | 13.47(84) | −1.02(85) |
| 2007–2019 | 7.15(17) | 13.71(11) | 19.25(73) | −2.52(73) |

**Table A2.** Errors budget on the position and the magnitude of the calculated proper motion vectors. The combined error refers to the fact that the proper motion further analysed in this study is the mean of the proper motion computed for the 2007–2016 and the 2007–2019 sets.

| Sets | Proper motion mas yr$^{-1}$ | | Position mas | |
|---|---|---|---|---|
| | Systematic | Random | Systematic | Random |
| 2007–2016 | 1.4 | 13 | 6.1 | 6.1 |
| 2007–2019 | 1.0 | 13 | 6.1 | 6.1 |
| Combined | 0.9 | 9.2 | 4.3 | 4.3 |

one where the entire Crab fits within a single Megacam chip). We used the PYTHON package REPROJECT (Robitaille, Deil & Ginsburg 2020) for this purpose. As the registration process does not involve non-linear geometric correction, the projection is robust and does not induce any small scale distortion. We used a flux-conserving spherical polygon intersection algorithm for the reprojection. The projected images were used to produce the layered image shown in Fig. 1.

### A2 Step 2: proper motion computation

Once the compared images are properly aligned we can obtain the proper motion in right ascension and declination at any given position by computing the displacement of the image in a small 20 × 20 pixel$^2$ tile (3.7 arcsec × 3.7 arcsec) around the chosen coordinates.

For this purpose, instead of directly using a FFT-based cross-correlation algorithm, which is faster but has numerous border effects on small regions, we explore a range of shift possibilities along the $x$ and $y$-axes on one tile and keep the one that shows the highest correlation with the reference tile. The highest correlation is found when the distance between both the shifted tile and the reference tile is minimal in least square terms. The loss function we try to minimize can be expressed as a $\chi^2(\Delta x, \Delta y)$ of two parameters: $\Delta x$ and $\Delta y$, resp. the $x$ and $y$ shift of the tile:

$$\chi^2(\Delta x, \Delta y) = \sum (I_{\mathrm{shift}}(\Delta x, \Delta y) - I_{\mathrm{ref}})^2 \ , \qquad \text{(A1)}$$

where $I_{\mathrm{shift}}(\Delta x, \Delta y)$ is the shifted tile and $I_{\mathrm{ref}}$ is the reference tile (see Fig. A1). Note that, before being compared the tiles are normalized and clipped at their respective 25th and 75th percentiles to mitigate the effects due to a different sky transparency or the variation of the sky background.

In principle a minimization algorithm could be used directly. But, because non-integer shifts rely on an interpolation algorithm that produces small distortions, we want to limit the shifts to integer values. Also, in order to avoid a local minimum, we use a brute force minimization. Shifts from −3.7 arcsec to +3.7 arcsec (approx. −2900 to 2900 km s$^{-1}$) in steps of 1 pixel 0.037 arcsec (or 0.187 arcsec i.e. approx. 150 km s$^{-1}$) in both $x$ and $y$ directions were attempted. This process yields a $\chi^2$ matrix where the global minimum can be securely found (see Fig. A1). The precision of this minimization can then be greatly enhanced by interpolating the $\chi^2$ matrix around the minimum with a 3rd order polynomial, the subpixel precision minimum being the minimum of this polynomial.

We have tested the precision of this algorithm on simulated data – a large gaussian (with a fwhm of 10 pixels) shifted by an arbitrary value – and we found that, in the ideal noiseless case, the shift of the gaussian could be retrieved with a precision of $5 \times 10^{-4}$ pixel. It is clearly not the precision that can be obtained on real data obtained under different conditions on a changing object, but the exercise demonstrates convincingly that it will not be limited by the algorithm.

Interestingly enough we found that the algorithm developed for this study was in fact very similar to the processing involved in Particle Image Velocimetry (PIV) used in the field of fluid mechanics to map fluid flows (see e.g. Keane & Adrian 1990; Adrian 1991; Thielicke & Stamhuis 2014) with the difference that the images analysed in PIV are made of numerous point-like objects. The method used to determine the most probable shift between two images generally relies on the maximization of a cross-correlation function,[1] while our method relies on the minimization of the quadratic distance. We tried both methods and found that the returned matrices (a cross-correlation matrix in the PIV case and a $\chi^2$ matrix in our case) were in fact very similar. The precision of both methods on our simulated data was nearly the same, though our algorithm yields a marginally better precision on a noiseless set of data.

The displacement vectors obtained with this algorithm should be, in principle, further corrected for residual local distortions unaccounted for during the registration step. But the relatively low precision on the estimation of the position of the individual stars compared to the quality of the registration makes this step unnecessary since the estimation of the local distortion field must

---

[1] In the PIV cases, equation (A1) would be replaced with

$$C(\Delta x, \Delta y) = \sum I_{\mathrm{shift}}(\Delta x, \Delta y) I_{\mathrm{ref}} \ . \qquad \text{(A2)}$$

logically depend on a small number of stars. However, the precision of the estimation based on e.g. five stars appears too low when compared to the precision of the large scale registration. We found that, a correction based on a small number of stars was in fact increasing the scattering of the data. We thus decided to rely on a much larger set of stars.

### A3 Step 3: corrections for systematics

Systematic biases in the calculated proper motions can greatly affect the position of the derived expansion centre (see Section 3). Over a ∼10 yr span, a relative shift of 0.1 pixel (19 mas) between the compared images translates to a proper motion shift of 1.9 mas yr$^{-1}$ and thus a final shift of the calculated expansion centre of 1.9″, given an expansion age of ∼1000 yr.

Multiple issues contribute to a systematic shift in the measured proper motion.

(i) Registration biases. In our case, the mean registration error is never higher than 0.02 pixel, i.e. 4 mas (see Section C) and was directly subtracted from the measured proper motion. But the uncertainty on this bias is comparatively higher and it must be accounted for in the error budget. Considering one standard deviation as the maximum systematic registration error, registration biases could contribute to a systematic shift of 0.07 pixel (≈12 mas) between the compared images.

(ii) Mean proper motion of the registration stars. As the stars are aligned during the registration, the mean proper motion of the stars used for the registration is added to the computed proper motion. Using the *Gaia* catalogue, we can estimate it and substract its contribution (see Table A1).

(iii) PSF asymmetries. Differences in the optics used, guiding errors, atmospheric conditions and other factors can modify the shape of the PSF. Any asymmetry will result in a systematic bias of the measured centroid which will eventually produce an additional registration shift. We have normalized and stacked together the stars used for the registration on a grid oversampled by a factor of 10 for every image of our data set (see Fig. A2). The resulting high SNR PSFs have subsequently been fitted with the same algorithm used during the registration in order to estimate the relative error made on the position of the centroid between the compared images.

(iv) Parallax. At a distance of 2 kpc, the maximum parallax is 0.5 mas which can be safely neglected given the magnitude of the preceding contributions.

### A4 Step 4: projection to celestial coordinates

The raw output of our algorithm is an estimate of the pixel displacement $(\mu_x, \mu_y)$ of a small region centred at the pixel coordinates $(x, y)$ between two images obtained at two different times $t_1$ and $t_2$. From there, given the parameters of a World Coordinate System (WCS) (Greisen & Calabretta 2002) that transform the pixel coordinates to celestial coordinates, the proper motion $(\mu_\alpha, \mu_\delta)$ is obtained as follow:

$$\begin{pmatrix}\alpha\\ \delta\end{pmatrix} = \mathrm{WCS}\begin{pmatrix}x\\ y\end{pmatrix} \tag{A3}$$

$$\begin{pmatrix}\mu_\alpha\\ \mu_\delta\end{pmatrix} = \left(\frac{1}{t_2 - t_1}\right)\mathrm{WCS}\begin{pmatrix}x+\mu_x\\ y+\mu_y\end{pmatrix} - \begin{pmatrix}\alpha\\ \delta\end{pmatrix}, \tag{A4}$$

$$\mu_\alpha^\star = \mu_\alpha \cos(\delta) \tag{A5}$$

With two sets of data to compare (the 2019–2007 set and the 2016–2007 set) that should give the same values, we can estimate the uncertainties on our method. If we look at the difference between the proper motion vectors obtained from the 2019 set and the 2016 set computed over the whole SNR (see Section 3), we see that the median difference is smaller than 2 mas yr$^{-1}$ and the standard deviation is around 13 mas yr$^{-1}$. Given the fact that the uncertainty found when comparing our data with that of T68 (see Section B) is around 10 mas yr$^{-1}$ (when combining the proper motion measured with the 2007–2016 and the 2007–2019 sets), we conclude that the measured uncertainty of 13 mas yr$^{-1}$ is a good estimate of the uncertainty of the proper motion vectors computed when comparing two images. When combining both sets, this error falls to 9.1 mas yr$^{-1}$. The complete error budget of our data is presented in Table A2.

## APPENDIX B: COMPARISON WITH TRIMBLE (1968)

T68 reported in her paper a table (Table II) of the 132 proper motion vectors she used in her analysis as well as their positions with respect to the central double star previously used by Duncan (1921) and later by N98 and K08. This star was well chosen as a reference as it displays a very small proper motion (see Table B1).

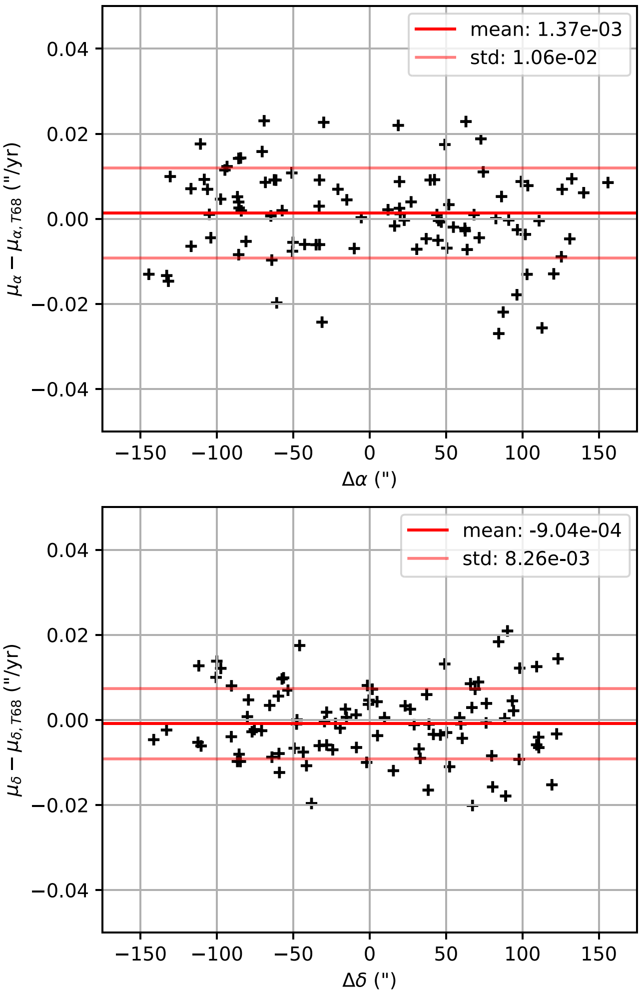

**Figure B1.** Difference with T68 on the measured proper motion along right ascension (top) and declination (bottom). The mean and standard deviation are indicated in each panel.

**Table B1.** Duncan (1921) Reference star coordinates and proper motion from *Gaia* DR3 (Gaia Collaboration 2016, 2023). Following T68 this star is the North following star of the central double star.

| Designation | *Gaia* DR3 3403818176867563264 |
|---|---|
| $\alpha$ (°) | $83.6341075 \pm 4.15\times10^{-5}$ |
| $\delta$ (°) | $22.0155339 \pm 3.45\times10^{-5}$ |
| $\mu_\alpha$ (mas yr$^{-1}$) | $2.291 \pm 0.202$ |
| $\mu_\delta$ (mas yr$^{-1}$) | $-5.382 \pm 0.130$ |

We may hence compare the proper motion we compute from our data at the positions chosen by T68. But we cannot simply look at the exact same coordinates since the Crab has since expanded and the regions considered by T68 are now a little farther away. We therefore estimated the actual coordinates of these regions from the measured proper motion, computed with respect to the estimated position of the reference star in 1966. The results of this comparison are summarized in Fig. B1. Note that this comparison is only correct from a statistical point of view because we did not try to find the exact same positions as the one used by T68. The idea behind this comparison is to rule out the possibility of any significant systematic error in our method and to obtain an upper limit on its precision.

The difference between the proper motions measured and those of T68 show a deviation $\lesssim 1.6\,\mathrm{mas\,yr^{-1}}$ with an uncertainty of $10\,\mathrm{mas\,yr^{-1}}$ which is very comparable to the uncertainties quoted in Section A4.

## APPENDIX C: RAW IMAGES REGISTRATION

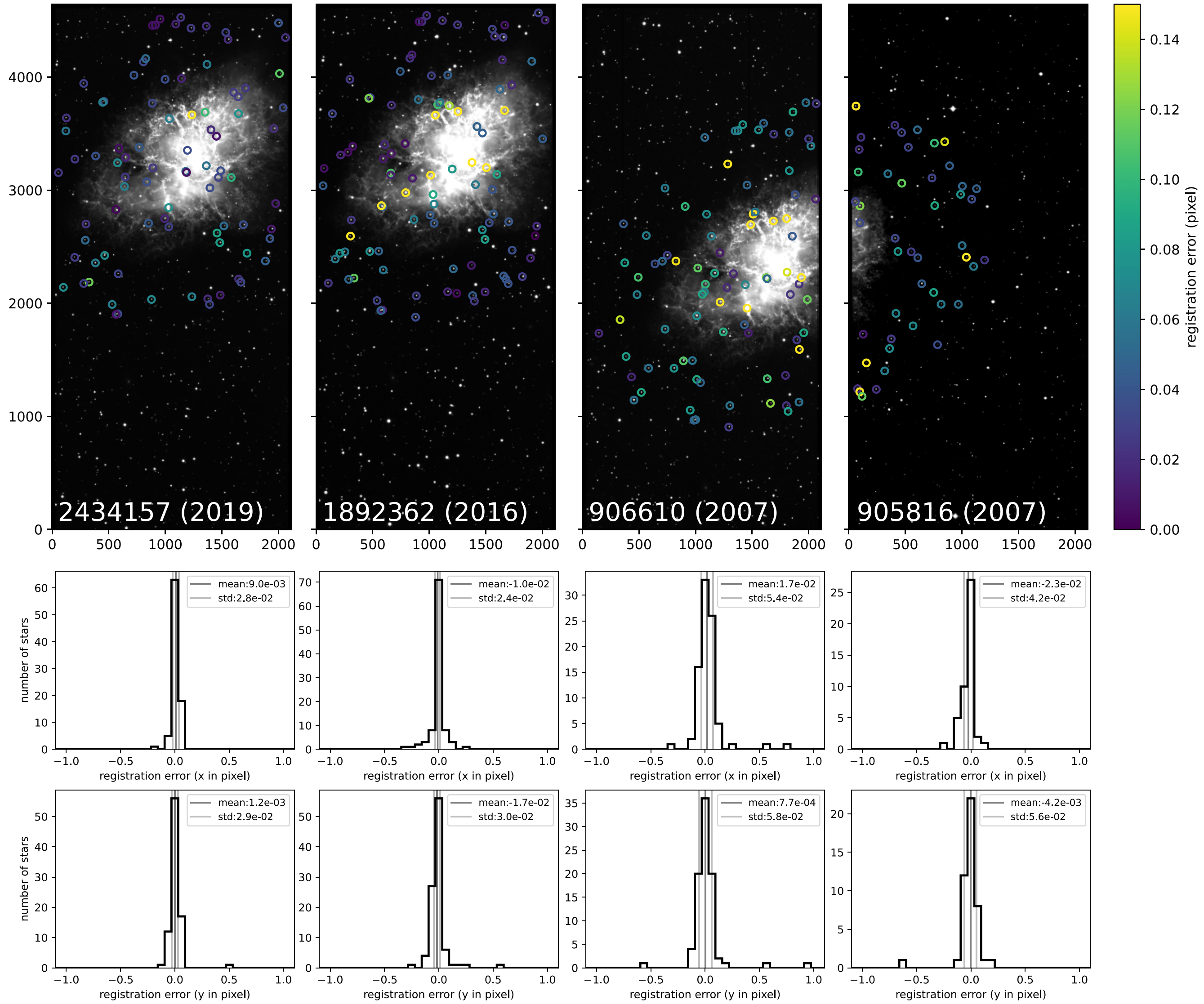

**Figure C1.** Images compared to compute the proper motion. The positions of the reference stars used for registration are shown as well as the registration error for each one of them. The distribution of the registration error along the *x* and *y* axes (roughly aligned with resp. the right ascension and declination) are shown in the panels below. The mean and standard deviation of the distribution are indicated.

This paper has been typeset from a TEX/LATEX file prepared by the author.